Computational Materials Science 95 (2014) 74–83

Contents lists available at ScienceDirect

Computational Materials Science

journal homepage: www.elsevier.com/locate/commatsci

Structural evolution of nanoparticles under picosecond stress wave consolidation

Chong Li, Kelsey Burney, Kevin Bergler, Xinwei Wang *

2010 Black Engineering Building, Department of Mechanical Engineering, Iowa State University, Ames, IA 50011, USA

ARTICLE INFO

Article history:
Received 9 May 2014
Received in revised form 15 July 2014
Accepted 18 July 2014

Keywords:
Nanoparticle consolidation
Cold-sintering
Nanocrystalline
Orientation–radial distribution function

ABSTRACT

In this work, large-scale atomistic modeling is conducted to explore a relatively cold consolidation process: nanoparticles compressed by a stress wave from a sacrificial layer that is ablated by a picosecond laser. The temperature, stress, atomic configuration, and crystallinity are studied in detail to understand the structural behaviors under extreme compression. Study of the temperature and structure evolution reveals that compression and reconstruction are cold processes indeed. Despite the destruction–reconstruction process, the material temperature is below its melting point. The stress wave consolidation leads to a final nanocrystalline structure. An orientation–radial distribution function (ODF) is designed to study the status of the nanocrystalline structure in detail. Compared with the radial distribution function, the ODF provides a 2D picture of the material structure, and uncovers details of material twisting and destruction. Smaller nanoparticles are easier to consolidate and reconstruct, and the final structure is more like amorphous and structural defects are observed. The center part of the particle retains its original crystalline structure while cold-consolidation primarily occurs in the particle–particle contact region. The number of reconstructed atoms is higher when the particle size is smaller, and strong structure twisting in space is observed.

1. Introduction

Due to the rapid development of the semiconductor industry and the wide spectrum of laser use in material processing, laser-material interaction has been a very active research area in recent decades. Laser ablation is a physical process used to generate nanoparticles free of contaminants like unreacted starting materials. Extensive research has been done to explore the use of pulsed laser ablation to control the quality of thin films made of nanoparticles and nanoparticle formation [1,2]. Zhigilei et al. did a systematic study of factors like laser fluence and pulse duration which play important roles in laser ablation [3]. Plech et al. found that gold nanoparticles ablation occurs below the particle's melting point [4].

As a byproduct of laser ablation, the high speed plume gives rise to shock wave in the ambient gas. Simulation works about the shock wave in laser-material interaction have been done by our group [5–8]. Recently, a transparent overlay was placed on the sacrificial material and specimen to induce a shock wave propagating downwards toward the specimen. Laser-induced compressive stress waves have the potential to compress micro/nanoparticles to form the desired structure. Zhang et al. have reported the microscale effects of laser shock wave used to obtain the desired residual stress patterns in microcomponents [9,10]. And Molian et al. have confirmed that the laser shock wave process can help with generating a strong, wear resistant, durable composite coating on aluminum [11]. In the past, laser shock peening (LSP) has been employed as a surface treatment of metals and was widely applied for turbine engine components. It has the advantage of improving surface properties of metallic components by introducing compressive residual stresses. Peyre et al. found that the pitting corrosion resistance of 316 L steel was improved after laser peening [12]. Lin et al. discovered that the combination of laser sintering (LS) and LSP contributes to better fatigue performance [13]. Finite element analysis has been applied to simulate the LSP procedure [14–16].

Laser induced plasma (LIP) produced in laser-material interaction has been used to remove nanoparticles and are used for the analysis of laser-induced breakdown spectroscopy (LIBS). LIP was found to be more effective by increasing pressure by an order of magnitude if LIP is constrained in a shock tube [17]. Similar spatial confinement effects on LIP have been explored extensively in Lu's group [18–20]. The interaction of nanoparticles with incident lasers is of great importance in the manufacturing field. Selective

* Corresponding author. Tel.: +1 515 294 2085; fax: +1 515 294 3261.
E-mail address: xwang3@iastate.edu (X. Wang).

http://dx.doi.org/10.1016/j.commatsci.2014.07.036
0927-0256/

laser sintering (SLS) sinters powders of microscale in a layer-by-layer style. Nanoparticle additive manufacturing has been proposed by Nair et al. as a novel solid freeform fabrication process [21]. In laser sintering, particles/powders will be melted, and then solidify to form a consolidated part. For environment or substrate that cannot sustain such high temperature (melting point of the powder), it becomes challenging to sinter powders on a substrate without severely damaging it.

This work is designed to numerically explore a new laser-assisted low-temperature consolidation method: using the stress wave generated by laser irradiation to compress nanoparticles to achieve cold sintering. This work is focused on exploring the structural transformation of nanoparticles under the effect of stress wave in pico-second laser material interaction. Cold sintering has advantages of consolidating powders of weak laser absorption or difficult to melt, or sintering nanoparticles on a substrate that cannot sustain a high temperature. We intend to investigate the various physical processes during stress wave-induced consolidation, in anticipation to unveil how the nanoparticle structure evolves to become dense.

2. Methodologies of simulation and the physical process under study

Molecular dynamics (MD) simulation tracks the trajectories of atoms and molecules by solving Newton's equation and could provide us with insight into the internal physical mechanisms in stress wave-induced material consolidation. It is employed in this work to investigate the nanoparticle consolidation process under laser irradiation. Argon is chosen as the material to be used in the simulation, due to its widely available potential, physical properties and significant computational cost reduction. Lennard-Jones potential (6–12 potential) is used to describe the interaction of atoms. For argon, the LJ potential well depth ε is 1.653×10^{-21} J and equilibrium separation parameter σ is 3.406 Å. The cut-off distance of the potential is 2.5 σ. Fig. 1(a) shows the initial atomic configuration of the sacrificial layer and arrays of nanoparticles with a diameter of 10 nm. The whole physical domain measures $91.6 \times 33.5 \times 22$ nm^3 ($x \times y \times z$). The sacrificial layer is 13.8 nm along the x direction and 29.8 nm, 19.8 nm in the y and z direction. This sacrificial layer is used to absorb the laser energy. Under irradiation, this layer will quickly vaporize, generating a very strong plume moving against the nanoparticle region. Under the strong compression of this plume, the nanoparticles are expected to reconstruct. Arrays of nanoparticles occupy the space of $59.8 \times 31.4 \times 20$ nm^3. The gap between the sacrificial layer and the top of the nanoparticles is approximately 15 nm to avoid the deformation of the sacrificial layer and nanoparticles resulting from their interaction during initial equilibrium state calculation. Nanoparticles of three different diameters (D = 5 nm, 8 nm, 10 nm) are studied in this work.

The arrangement of nanoparticles is similar to the hexagonal close packed (HCP) crystal structure. Each nanoparticle of diameter D occupies one point of the HCP structure and the nanoparticles are tangential to the nearest neighbors. All the particles follow the same crystographical orientation in the initial structure. This eases our study and analysis of the crystalline destruction by the consolidation process. To constrain the movement of atoms, wall potential (wall/LJ93) is implemented in the six boundaries. The strength factor ε for wall-particle interaction is 1.653×10^{-21} J and the size factor σ is 3.615 Å in this work. 8.515 Å is chosen as the cutoff distance for the wall boundary. 5 fs is chosen as the time step for the simulation. The LAMMPS package is used to carry out the simulation [22]. First, the whole system is thermostated at temperature T = 50 K for 4 ns as a canonical (NVT) ensemble. Then the system is run as a microcanonical (NVE) ensemble for 500 ps to damp the disturbance introduced to the system during the NVT

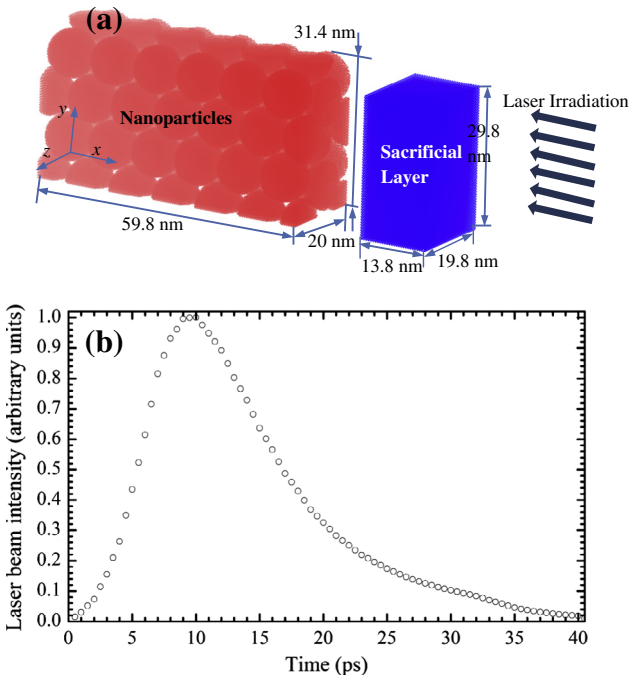

Fig. 1. (a) Schematic of the physical domain under simulation. The blue region is the sacrificial layer to absorb the laser energy, and the red region is argon nanoparticles (10 nm diameter) to be compressed (cold-sintered). The whole simulation box measures $91.6 \times 33.5 \times 22$ nm^3 ($x \times y \times z$). The size of nanoparticle region is $59.8 \times 31.4 \times 20$ nm^3 ($x \times y \times z$). The size of the sacrificial layer is $13.8 \times 29.8 \times 19.8$ nm^3 ($x \times y \times z$). The gap between the sacrificial layer and nanoparticles is approximately 15 nm. A potential wall boundary is applied to the six walls of the simulation box. Laser irradiation is applied in the negative x direction. (b) Temporal profile of the picosecond laser pulse used in the simulation. The FWHM of the pulse is 11.5 ps, and the peak is located at 9 ps. (For interpretation of the references to colour in this figure legend, the reader is referred to the web version of this article.)

calculation. The thermal equilibrium is confirmed to be reached after the 500 ps NVE run.

Laser energy with a temporal distribution as seen in Fig. 1(b) irradiates the sacrificial layer surface afterwards. The full width at half maximum (FWHM) of the incident laser beam intensity distribution is 11.5 ps and peaked at 9 ps. The laser energy comes in the negative x direction. Laser energy is absorbed volumetrically in the sacrificial layer and the absorption process obeys the Beer–Lambert law. In the simulation, the laser energy is absorbed in a layer-by-layer way and it is only absorbed by the sacrificial layer. To implement it, the sacrificial layer is divided into bins of thickness δx = 1 nm along the x direction. The absorption in each layer can be expressed as

$$\Delta E = E[1 - \exp(\delta x/\tau_0)], \tag{1}$$

where τ_0 is the adjusted real optical absorption depth and calculated as $\tau_0 = \tau \cdot \rho_0/\rho_1$. ρ_0 and ρ_1 are the densities of the bin and the whole target, respectively. τ is the absorption depth and in this work τ = 5 nm. The velocity of each atom is rescaled at every time step as

$$V'_{i,j} = (v_{i,j} - \bar{v}_j)\chi + \bar{v}_j, \tag{2}$$

where $v'_{i,j}$ is the new velocity for atom i and $v_{i,j}$ and $\bar{v}_j$ is the velocity of atom i at this time step and the average velocity of atoms of the bin in the x, y, z directions and the rescaling factor χ is calculated as

$$\chi = \left\{1 + \Delta E / \left[0.5 \sum_{i=1}^{N} m_i \left[(v_{i,1} - \bar{v}_1)^2 + (v_{i,2} - \bar{v}_2)^2 + (v_{i,3} - \bar{v}_3)^2\right]\right]\right\}^{0.5}. \tag{3}$$

Our above laser absorption treatment ensures that only the thermal movement of atoms is excited upon laser irradiation, while the overall momentum of the system is conserved.

3. Results and discussion

3.1. Temperature and stress distribution and evolution during compressing

In nanoparticle consolidation, temperature and stress are two critical factors that influence the structure evolution. First of all, we show pictures to illustrate how the nanoparticles are compressed by the strong stress wave from the sacrificial layer. Then the temperature and stress are studied. Fig. 2 shows the general picture of the consolidation process for case $D = 10$ nm, $E = 2.7$ mJ/cm^2. To have a clear view, a slab ranging from $z = 9$ nm to 9.5 nm was taken out to generate the atomic snapshots. In the beginning, the laser energy is absorbed by the sacrificial layer. Then the sacrificial layer begins to melt under the laser irradiation. Due to the constraint of the top and side potential walls, the sacrificial layer is pushed towards the top surface of nanoparticles. This is shown in Fig. 2 at $t = 40$ ps. 65 picoseconds after laser irradiation, the sacrificial layer is in touch with the nanoparticles. Afterwards, the nanoparticles start to be compressed and crushed from the top to bottom gradually. The sacrificial-layer atoms concentrate on the top surface of the nanoparticles and very few atoms are observed to be embedded in the nanoparticle array. Finally, nanoparticles are deformed into amorphous/nanocrystalline (termed "destructed" structure in this work) state as that shown at $t = 300$ ps in Fig. 2.

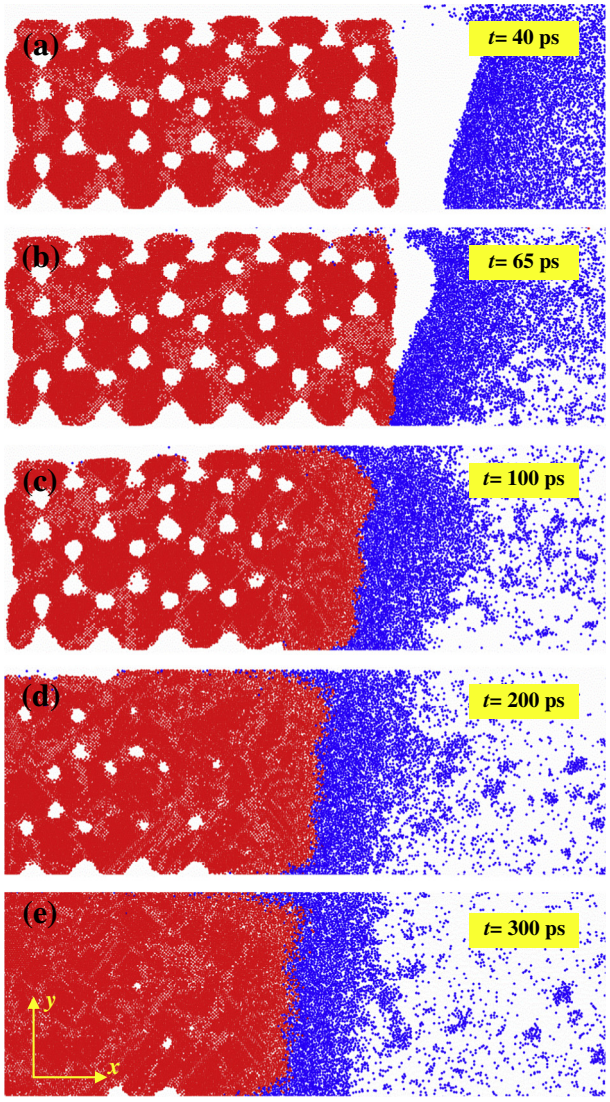

Fig. 2. Snapshots for compressing of nanoparticles with $D = 10$ nm. The laser fluence is $E = 2.7$ mJ/cm^2. From $t = 40$ ps to 65 ps, the sacrificial layer melts and is pushed down towards the top of nanoparticles. At $t = 100$–300 ps, the nanoparticles are compressed. At the end of 300 ps, the nanoparticles are almost destructed completely.

Temperature and stress contours are plotted to explore their distribution and evolution during the compressing process. Fig. 3(a) and (b) shows the temperature and stress contours for the case illustrated in Fig. 2. Before the consolidation starts, nanoparticles are in a state of equilibrium and the temperature is uniform around 50 K as shown at the initial moments in Fig. 3(a). As time progresses, the consolidation process is accompanied by a quick temperature rise. Heat is transferred from the high-temperature sacrificial layer to the nanoparticles array. And it contributes to the fast collapse of the nanoparticles. This heat transfer is considered naturally since MD simulation models the movement and interaction of atoms. Therefore, the energy exchange among atoms is considered all the time. Noticeably, a high temperature is supposed to be transferred from the top surface to the bottom in the consolidation process. However, as shown in Fig. 3(a), instead of straight slope line, the temperature contour line is shown with a hump as marked in Fig. 3(a). This means there is heat transferred from the bottom towards the inside. Since the bottom is fixed with the potential wall, the compression near the bottom surface accounts for the temperature rise. This can also be validated by the spots of the high compression force shown in Fig. 3(b). As a consequence, the temperature of the bottom part close to the potential wall is a little bit higher than that in the middle part. In general, the high temperature will go down gradually with the consolidation process. In Fig. 3(a), the large green region of the material after about 250 ps is around 67 K, lower than the melting point of Argon: 83.8 K. Considering the high pressure existing in the material, the melting point should be even higher than 83.8 K. This indicates that under the rapid pressure consolidation induced by the stress wave, the argon nanoparticles experience structure damage and reconstruction, rather than melting and solidification.

Fig. 3(b) is the stress contour of nanoparticles in the consolidation process. The stress refers to the normal stress and is calculated as $\sigma = (\sigma_{xx} + \sigma_{yy} + \sigma_{zz})/3$. Similar to the temperature distribution, the compressive stress will move from the top surface to the bottom quickly, but also experiences damping. Before $t = 45$ ps, no obvious compressive stress is observed. Afterwards, around $t = 70$ ps, the first spot (Spot 1) under big compression force shows up. This is exactly the time when the sacrificial layer touches the nanoparticles and starts to compress them. Part of the compressive stress is released by the structure collapse of the top nanoparticles. However, part of the compressive stress manages to go deep down into the nanoparticles arrays. Interestingly, another big compression spot (Spot 2) appears around the time $t = 275$ ps. This is induced by the compression at the bottom. Finally, at approximately $t = 325$ ps, the particle structure is completely destroyed and the compressive stress begins to be released from that time.

The crystal structure is a key criterion to judge the state of nanoparticles at the atomic level. And crystallinity is the index to show that the particles are close to the perfect crystal state or away from the perfect crystal structure. In this work, crystallinity is defined as [23,24]:

$$\phi(r_{i,x}) = \frac{1}{N}\left|\sum_i e^{j2\pi(2r_{i,x}/\lambda)}\right|, \tag{4}$$

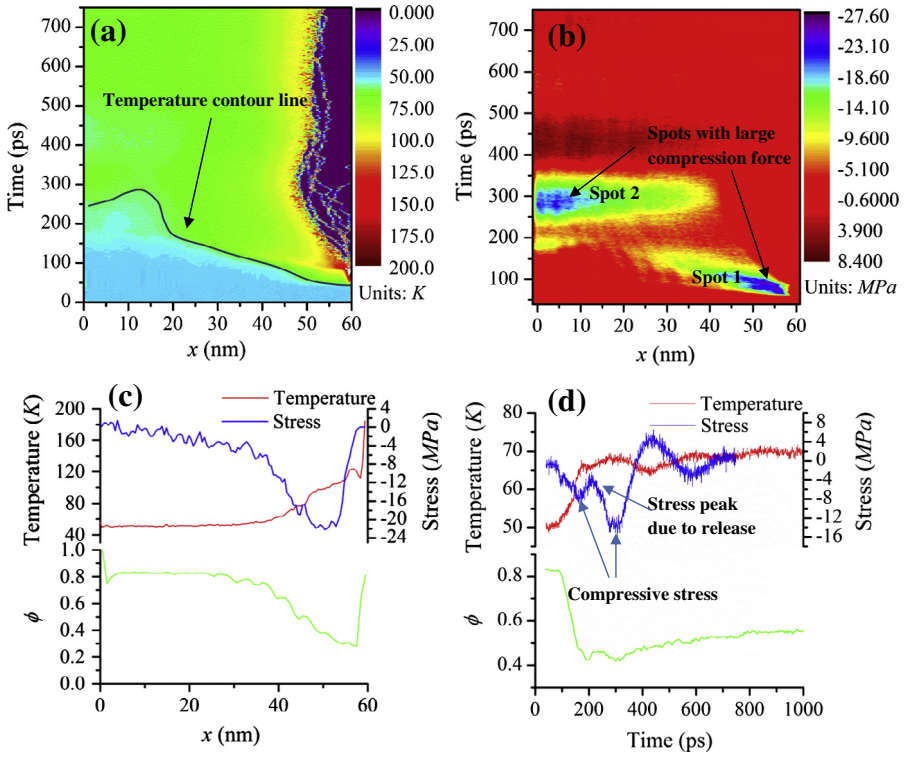

Fig. 3. (a) Spatiotemporal temperature distribution for nanoparticles with $D = 10$ nm during laser-induced stress wave consolidation ($E = 2.7$ mJ/cm^2). A temperature contour line is given for the convenience of telling the change of temperature for different parts of nanoparticles with time. (b) Stress contour for the case $D = 10$ nm, $E = 2.7$ mJ/cm^2. The stress refers to the normal stress and is calculated as $\sigma = (\sigma_{xx} + \sigma_{yy} + \sigma_{zz})/3$. Two spots with large compression force are pointed out. Spot 1 is due to the compression of sacrificial layer and spot 2 results from the constraint of the bottom potential wall. (c) Temperature, stress, crystallinity against location x at time $t = 100$ ps. The stress peak is accompanied by a sharp drop of crystallinity afterwards. (d) Temperature, stress, crystallinity against time at location $x = 25.35$ nm.

where $r_{i,x}$ is the x coordinate of atom i and λ is the light wavelength for crystallinity characterization. Here we assign λ with the value of the lattice constant $a = 5.414$ Å. $2r_{i,x}$ is the light travel distance from $x = 0$ and then comes back. If atoms are regularly distributed in space with their spacing in the x direction equal to $n(a/2)$, the function will be equal to 1. In the amorphous state, the function $\phi(r_{i,x})$ will be much less than 1, in fact very small (close to zero). The nanoparticles are divided along the x direction into layers with $\Delta x = 10$ Å. Each layer is then divided into cubes of 10 Å size, and the crystallinity of each cube is calculated. The crystallinity of each layer is the average of the crystallinity of all the cubes in it.

Fig. 3(c) is the temperature, stress and crystallinity at time $t = 100$ ps. Fig. 3(d) is the temperature, stress and crystallinity evolution at $x = 25.35$ nm against time. In Fig. 3(c) and (d), it can be seen that when the stress wave passes by, the crystallinity drops dramatically. This strongly confirms the structure damage by the high compressive stress. The high temperature moves from the top surface to the bottom nanoparticles. Because of the high laser fluence ($E = 2.7$ mJ/cm^2) in this case, the atoms around $x = 25.35$ nm experience a sudden temperature rise around $t = 180$ ps and then stay at the plateau value of $T = 67$ K (shown in Fig. 3(d)). The stress evolution in Fig. 3(d) shows the nanoparticles around $x = 25.35$ nm are compressed from $t = 77$ ps to 380 ps, which peaks at $t = 300$ ps. At 300 ps, the compressive stress reaches the highest level, explaining why the crystallinity is the worst at that moment. In Fig. 3(d), the temperature rise around 180 ps releases part of the compressive stress which is shown as a small peak in Fig. 3(d). It is obvious that the crystallinity drops following the compressive stress. This reveals the close relationship between the compression force and the structure destruction.

3.2. Structure evolution during nanoparticle compressing

As mentioned above, the crystallinity's value strongly reflects the structure of the material: a value close to 1 indicating crystalline structure close to the original one (we call this the "retained" structure), and a low value meaning destructed structure or severe structure damage. Note this "destructed" structure could mean either amorphous, or the lattice is strongly twisted from the original orientation. Fig. 4(a) shows the contour of the crystallinity of the nanoparticles for the case discussed in Fig. 3. There is a black line marked as crystallinity drop line in this figure. Below the black line, the crystallinity is very close to 1 which means sound crystalline structure. Above the crystallinity drop line ϕ is dropped to around 0.5. It should be noted that the crystallinity contour above 50 nm ($x > 50$ nm) at the late stage ($t \geqslant 100$ ps) is not reliable when the nanoparticles are compressed, since there may be one or just a few atoms in some layers above 50 nm. Noticeably, the compression force from the potential walls also contributes to the destruction of the structure of the nanoparticles at the bottom. As marked in Fig. 4(a), directly above the crystallinity drop line, the constraint from the potential walls plays an important role in destroying the structure completely. The effect of potential walls is also obvious when it comes to the cases with less laser fluence as shown in Fig. 4(b) and (c).

Fig. 4(b) is the crystallinity contour for the case $D = 10$ nm, $E = 2.0$ mJ/cm^2. In contrast with Fig. 4(a), the crystallinity drop line in Fig. 4(b) is in a hump shape. The crystallinity is below 0.5 at the bottom part around $t = 300$ ps. However, in the middle part ranging from $x = 16$ nm to 22 nm, the average crystallinity is above 0.6. The case $D = 10$ nm, $E = 1.5$ mJ/cm^2 has this similar observation, too (Fig. 4(c)). In Fig. 4(c), although the crystallinity of nanoparticles

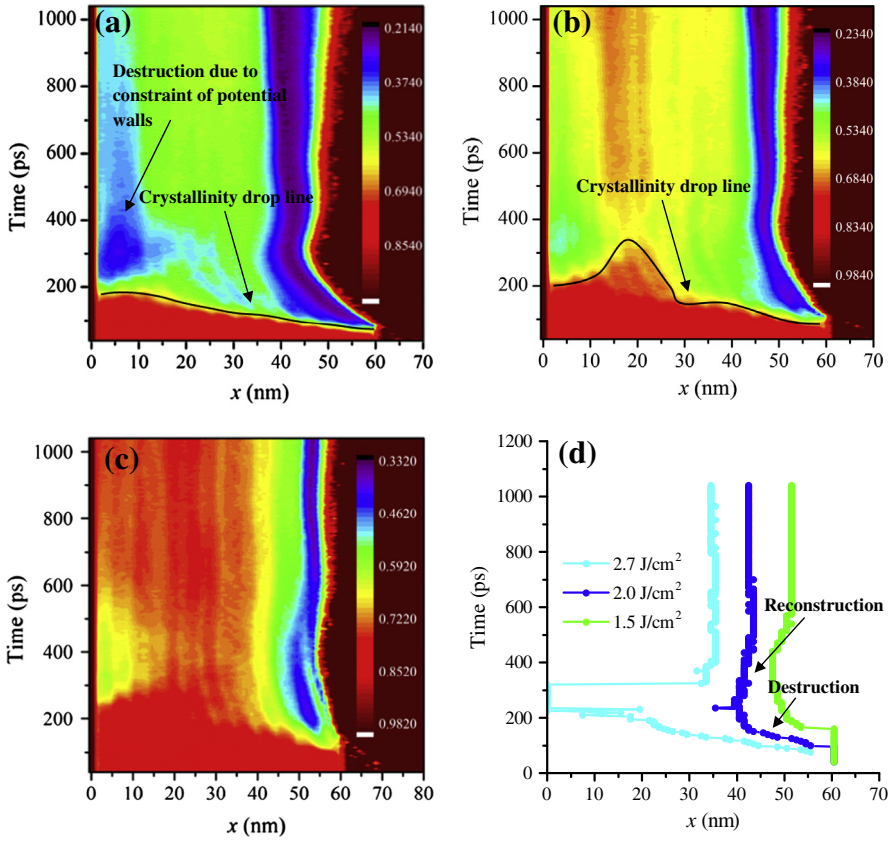

Fig. 4. Spatiotemporal contour of structure crystallinity for argon nanoparticles of $D = 10$ nm under compressing by laser fluence of (a) 2.7 mJ/cm^2, (b) 2.0 mJ/cm^2, and (c) 1.5 mJ/cm^2. In (a) and (b), the crystallinity drop line is quite distinguishable and is marked using a solid curve. Below the line, the crystallinity ϕ is approximately 1, while above the line ϕ is around 0.5. (d) Retained-destructed interface evolution against time. For $E = 2.7$ mJ/cm^2, the interface goes down quickly because the nanoparticles are completely destroyed. After that the reconstruction process occurs. For $E = 2.0$ mJ/cm^2 and $E = 1.5$ mJ/cm^2, only part of the nanoparticles are completely destroyed. After the reconstruction, the interface will be stable at $x = 42$ nm and $x = 52$ nm, respectively.

at the bottom is above 0.5, the crystallinity in the range $x = 16$–30 nm is apparently higher than the bottom part, which means the middle part of the crystal structure is more well preserved than the bottom nanoparticles. So it is conclusive that the compression in the bottom part plays a critical role in damaging the particles close to the bottom.

Fig. 4(d) shows the retained-destructed structure interface which is identified by the crystallinity ϕ of each layer. Comparing Figs. 3 and 4(a), along the crystallinity drop line, the temperature of the nanoparticles are still well-below the melting point. So the process is more like stress-induced structure change rather than a melting procedure. If ϕ of a layer is less than 0.5, it is defined as the destructed region in this work. Otherwise it is viewed as the retained part. Interestingly, for the case $D = 10$ nm, $E = 2.7$ mJ/cm^2, the top, middle and bottom parts are initially crushed into a destructed state. On the other hand, after time $t = 400$ ps, the crystallinity goes back to being above 0.5 for the middle part. As a result, two retained-destructed interfaces show up along the time. Fig. 4(d) plots the retained-destructed interface that is closer to the top surface. Until this point, we can draw a conclusion that nanoparticle consolidation consists of two processes: plastic and elastic. The plastic compressing gives a permanent final amorphous/nanocrystalline structure. The elastic compressing is responsible for the temporary structure damage, and such damage will disappear after the stress wave is released. Such temporary structure damage has been observed in our past work on laser-material interaction that involves melting and solidification [23,25].

The crushing process does not generate enough heat that makes temperature of all the nanoparticle atoms rise above the melting point $T_m = 83.85$ K. As in the case where $D = 10$ nm, $E = 2.7$ mJ/cm^2, the temperature in the middle part is around 65 K. As a result, the observed crystalline reconstruction after consolidation is not re-solidification. As shown in Fig. 4(d), the retained-destructed interface for the three cases all experience processes that involve damage moving deep down towards the bottom at first and then coming back towards the top surface (crystalline reconstruction) and finally staying in a plateau value. The dropping down part is the structure damaging process and the rising part represents the reconstruction process. The nanoparticles are completely destroyed so the retained-destructed interface will decrease dramatically and finally vanishes for the case $D = 10$ nm, $E = 2.7$ mJ/cm^2. After that, at approximately $t = 320$ ps, reconstruction begins from the middle part ($x = 32$ nm) of the crystalline region. The crystalline part will then expand. For cases $D = 10$ nm, $E = 2.0$ mJ/cm^2 and $D = 10$ nm, $E = 1.5$ mJ/cm, the crystalline reconstruction is observed from $t = 200$–600 ps and not all the nanoparticles are crushed down into destructed states in these two cases.

3.3. Effect of particle size and laser energy

The above discussed nanoparticle consolidation process is for particles of 10 nm diameter. It is expected that the process itself could vary a lot if particles of different sizes are present. Here the size of nanoparticles is varied to study the size effect. We use another two different particle sizes: $D = 5$ nm and 8 nm. Fig. 5(a) and (b) are the crystallinity contour for cases $D = 5$ nm and $D = 8$ nm with the same laser fluence, $E = 2.7$ mJ/cm^2. This structure contour is intended to explore how the structure evolves

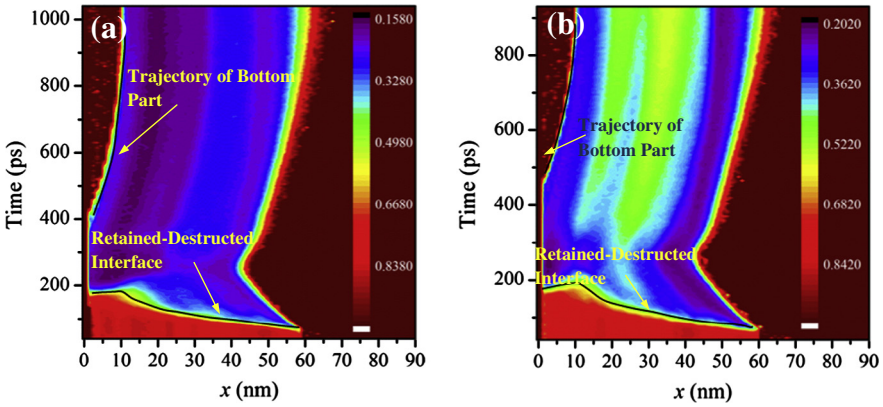

Fig. 5. Spatiotemporal contour of crystallinity for nanoparticles of different sizes: (a) $D = 5$ nm under laser fluence of 2.7 mJ/cm^2. (b) $D = 8$ nm under laser fluence of 2.7 mJ/cm^2. In both cases, the bottom parts of the nanoparticles are pushed back by the wall towards the top surface, as indicated by the trajectory of the bottom part in the figure. This is obvious by comparison between Figs. 4(a) and 5(a) and (b) in this figure. It is shown that when the particle size is bigger, this push-back effect becomes weaker.

during stress wave consolidation. For size $D = 5$ nm, the bottom nanoparticles are pushed back towards the top surface at $t = 400$ ps. For size $D = 8$ nm, this happens at $t = 460$ ps. However, no pushing-back is observed for nanoparticles of size $D = 10$ nm. During the particle consolidation process, a shear stress can be easily established at the particle–particle contact region. When the diameter of the nanoparticles decreases, the number of nanoparticles will increase for the same volume under study. Specifically, the arrangement of nanoparticles of size $D = 5$ nm indicates that there is more shear stress in the contact part of the nanoparticles (due to the dramatically increased surface-to-volume ratio). Compared with $D = 10$ nm and $D = 8$ nm, much less energy is needed for destruction and the extra energy will give rise to the pushing back process in the case of $D = 5$ nm. As shown in Fig. 5(a) and (b), for $D = 5$ nm, the crystallinity value drops more quickly and the average crystallinity is obviously lower than $D = 8$ nm. In addition, it is also found that the downward movement velocity for case $D = 5$ nm dissipates slower than the cases $D = 8$ nm and $D = 10$ nm. Finally, the pushing back process occurs earlier for the case $D = 5$ nm, $E = 2.7$ mJ/cm^2.

A specific moment $t = 1.04$ ns (the final stage of our simulation) is chosen for the comparison of atomic snapshots and is shown in Fig. 6(a)–(e). This comparison will help reveal how the final material structure looks and how it is affected by the particle size and laser energy. Fig. 6(a)–(c) are for comparison to explore the particle size effect, and Fig. 6(c)–(e) shows the effect of laser fluence for the cases of $D = 10$ nm. Comparing Fig. 6(a)–(c), we can conclude that a smaller particle size is more favorable for the compression destruction because of more contact surface among particles and more accumulation of shear stress as discussed above. Structure defects due to the atomic dislocation are marked in Fig. 6(a). These defects follow an angle of about 45° with respect to the laser incident direction. It is in this direction (45°) that the maximum shear stress exists, and this stress causes the structural defect. It also has been observed that the defect line is 45° with respect to the laser irradiation direction in our previous work [23,25]. The corresponding crystallinity (ϕ) contours are plotted in Fig. 6(f)–(j) for the convenience of comparison and analysis.

Small-size nanoparticles are easily crushed into the destructed state as shown by Fig. 6(f)–(h). The smaller the particles are, the lower the average crystallinity is. And the high laser fluence also contributes to the destruction of nanoparticles. A higher laser fluence leads to more deformation of nanoparticles. Fig. 6(h)–(j) are for the same particle size, but with different laser fluence. The sacrificial layer gains more energy in the higher laser fluence situation. The downward momentum is much stronger and finally results in the more serious collapse process of nanoparticles. Comparison between Fig. 6(h) and (j) shows that when the laser fluence is smaller, the nanoparticles cannot be compressed tightly to form a fully dense structure. At the nanoparticles arrangement level, voids/pores do exist in the final structure although the nanoparticles are closely connected (Fig. 6(e)). For the solid region, great crystallinity is preserved during consolidation, as indicated in Fig. 6(h)–(j).

3.4. Nanocrystalline structure after consolidation

Even though the crystallinity function shows how badly the crystal structure is destructed, we do not know whether the crystal is partially amorphous or just orientationally twisted. For smaller particles, during consolidation, they are easily twisted and are ready to change the crystallographic orientation to accommodate the impact from the stress. Therefore, the final structure could be more nanocrystalline-like with significant crystallographic orientation variation in space. And we believe this gives a smaller crystallinity function value as shown in Fig. 6(f). When the particles become larger, they are reluctant to be twisted and could retain some original crystallographic orientation. Therefore, a higher value of the crystallinity function is observed in Fig. 6(h). To confirm this explanation, an orientation–radial distribution function (ODF) is developed in this work for the first time. Similar to the radial distribution function (RDF), ODF reveals the atom density distribution as a function of the distance to the reference atom in the 3D space. Furthermore, it provides the angle information which is missing in RDF: the relative direction of the atoms to the reference one. The Euler angles show us the 3D space orientational arrangement of structure. The angle information in the $x - y$ plane is good enough to demonstrate how severely the structure is twisted in space at the atomic level in this work. To simplify the calculation work, only angle information in the $x - y$ plane is discussed here. The angle is defined with respect to the x axis and it is designated to be in the range 0–180°.

For simplicity, only the atom number is used for the analysis. Fig. 7(a) is the 3D image of the face-centered cubic (fcc) structure and Fig. 7(b) is the structure projection in the $x - y$ plane. In this fcc crystal cell, atom 2, 3, 4 are the 1st order nearest atoms to atom 1 as shown in Fig. 7(a). In our ODF computation, the atomic distance is obtained from the 3D space, while the angle is calculated with all the atoms projected to the 2D plane ($x - y$ plane). As shown in Fig. 7(b) the angles to the x axis are 0°, 45°, 90° for the nearest distance atoms. Since the unit cell is repeated along the x and y axis and the angle in ODF is defined in [0°, 180°], the angles

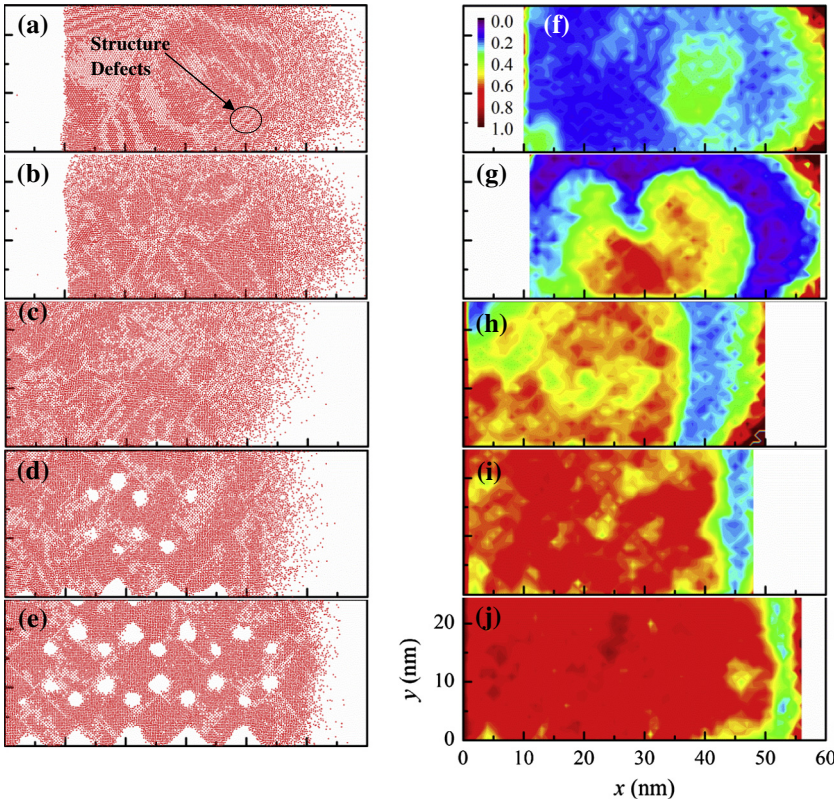

Fig. 6. Atomic configuration and contour of the crystallinity function at $t = 1.04$ ns to illustrate the effect of particle size and laser fluence. The y axis ranges from 0 to 25 nm. The x axis is from 0 to 60 nm. The simulation box size is a little bit different for cases with different particle diameters. For the cases with $D = 10$ nm, the simulation box is $91.6 \times 33.5 \times 22$ nm^3 ($x \times y \times z$) while for the cases with $D = 5$ nm (with 783,419 atoms) and $D = 8$ nm (with 763,760 atoms), the simulation box is $92 \times 26.6 \times 23.6$ nm^3 ($x \times y \times z$). Only atoms between $z = 9$–9.5 nm are plotted in the figures. (a) $D = 5$ nm, $E = 2.7$ mJ/cm^2; (b) $D = 8$ nm, $E = 2.7$ mJ/cm^2; (c) $D = 10$ nm, $E = 2.7$ mJ/cm^2; (d) $D = 10$ nm, $E = 2.0$ mJ/cm^2; (e) $D = 10$ nm, $E = 1.5$ mJ/cm^2. The final structure position of the case $D = 5$ and 8 nm is a little bit to the right of the wall due to the bouncing-back movement described in the text. For ϕ calculation, the simulation box is divided in the x and y direction with a size of 1 nm. Then the cube volume of the cases $D = 5$ nm and $D = 8$ nm is $1 \times 1 \times 23.6$ nm^3 and is $1 \times 1 \times 22$ nm^3 for cases $D = 10$ nm. (f) $D = 5$ nm, $E = 2.7$ mJ/cm^2; (g) $D = 8$ nm, $E = 2.7$ mJ/cm^2; (h) $D = 10$ nm, $E = 2.7$ mJ/cm^2; (i) $D = 10$ nm, $E = 2.0$ mJ/cm^2; and (j) $D = 10$ nm, $E = 1.5$ mJ/cm^2.

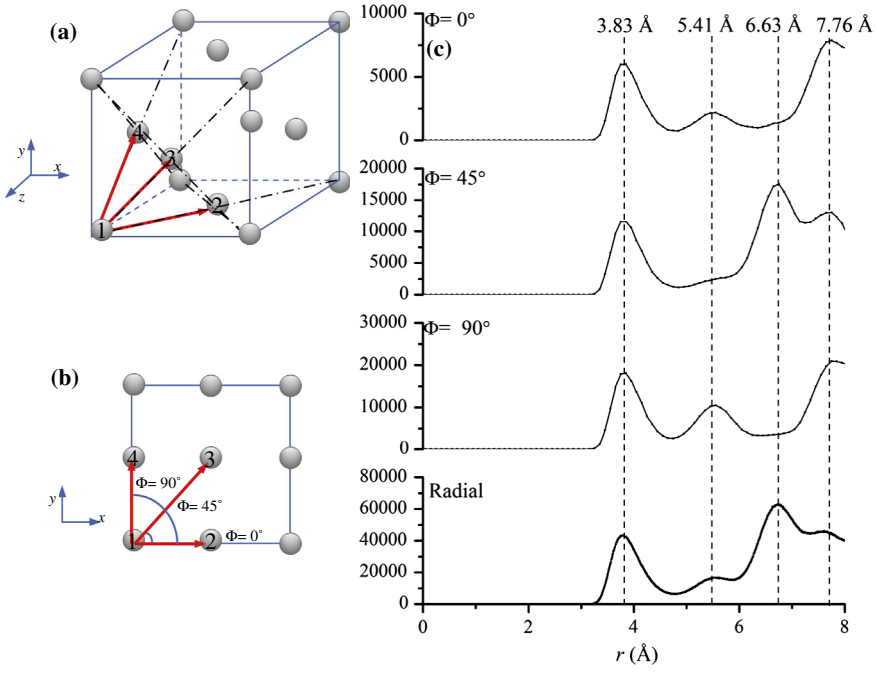

Fig. 7. (a) The structure of fcc crystal in 3D space. The 1st order nearest atoms to atom 1 are atom 2, 3 and 4. The 1st nearest distance is 3.83 Å; (b) the projection of fcc structure in the $x - y$ plane. The angles are 0°, 45°, 90°. The unit cell is extended along the x and y axis. So the angles are 0°, 45°, 90°, 135°, 180°; and (c) atom number variation with atomic distance. The y axis is the atom number within every 0.1 Å spacing along $\phi = 0°$, 45°, 90° and 0.00852 Å for radial (RDF).

for the 1st order nearest atom distance are 0°, 45°, 90°, 135° and 180° in ideal situations. Fig. 7(c) is the atom number variation as a function of the distance in different ODF angles. At $\phi = 0°$, the first peak is 3.83 Å. The second peak is 5.41 Å. Interestingly, since the atom–atom connection line of length 6.63 Å cannot be projected parallel to the x axis in the $x - y$ plane, so there is no peak in 6.63 Å. Then the third peak is 7.76 Å. The RDF can only give us the radial distribution information as shown in Fig. 7(c). However, the ODF includes the information about the atom density variation in different angles, and gives twisting details as shown in Fig. 8. In this work, in the ODF(r, ϕ), r refers to the atom–atom distance in 3D space while ϕ is the angle projection of the atom–atom connection in the $x - y$ plane.

Fig. 8 is the atom ODF polar contour. Before the laser energy is applied, the ODF of the 5 cases is similar to each other as shown by Fig. 8(a), (c), (e). The spots with a larger atom number are distributed at certain radii which correspond to the 1st–4th nearest atom distance (3.83 Å, 5.41 Å, 6.63 Å, 7.76 Å). Furthermore, the speckles in Fig. 8(a), (c), (e) are well located around certain angles. This proves that the structure at the initial state is very close to the perfect crystal structure. However, the ODF of the final state of the 5 cases differs a lot. Fig. 8(b), (d), (f) share the same laser fluence ($E = 2.7$ mJ/cm^2), but their particle size varies. For the case with a smaller particle size, like Fig. 8(b) ($D = 5$ nm), the distribution contour in the 1st, 2nd, 3rd and 4th nearest atomic distance is blur. Furthermore, the angle range in the above distance is broad. The angle in the 1st nearest distance is twisted. The angle should be in 0°, 45°, 90°, 135°, 180° for non-twisted crystal. However, in Fig. 8(b), the angle is 0°, 60°, 120°, 180°. Since the shear stress in the angle 45° and 135° is the largest one, materials are more likely to be twisted to other angles. For a large particle size, like Fig. 8(f) ($D = 10$ nm), the distribution contour is much clearer. At the 1st nearest atomic distance, the angles are well located in 0°, 45°, 90°, 135°, 180°. For the case $D = 8$ nm, $E = 2.7$ mJ/cm^2, the distribution contour is blur but well located at the corresponding angles. We can conclude its destruction level should be between the case $D = 5$ nm, $E = 2.7$ mJ/cm^2 and the case $D = 10$ nm, $E = 2.7$ mJ/cm^2.

Fig. 8 (f), (g), (h) demonstrate the effect of laser fluence. They are all for the same size of particles: $D = 10$ nm. For the case with a less laser fluence ($D = 10$ nm, $E = 1.5$ mJ/cm^2), the atom distribution in 1st–4th nearest distance is well located around the corresponding angle. The contour is much clearer than the case with $D = 10$ nm, $E = 2.7$ mJ/cm^2 and the angle distribution is less broad.

The angle variation with the atom–atom distance after consolidation for $D = 10$ nm, $E = 2.7$ mJ/cm^2 is explored for the analysis as shown in Fig. 9. The 1st nearest distance is 3.83 Å. As we refer to Fig. 9, the angle should be 0°, 45°, 90°, 135°, and 180°. The 2nd nearest distance is 5.41 Å, and the angles are 0°, 90° and 180°.

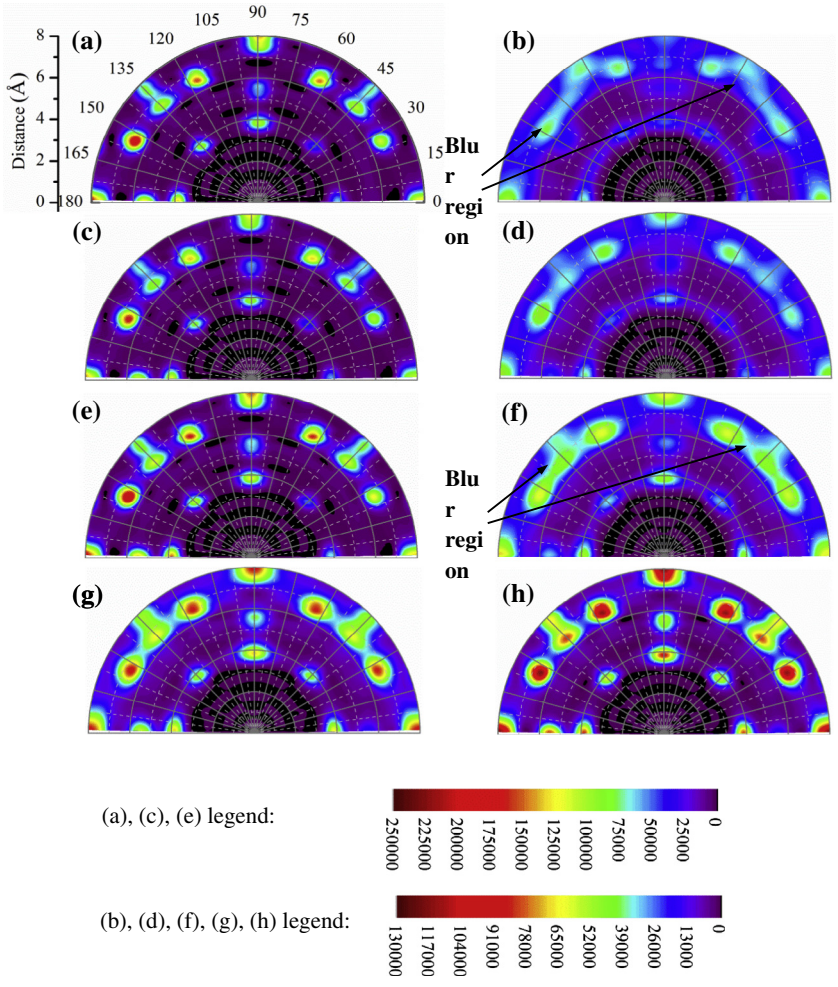

Fig. 8. Polar contour of the orientation–radial distribution function (ODF). The calculation is conducted in the $x - y$ plane. The angle is the one between the line connecting the two atoms and the x axis. It is defined to range from 0 to 180°. The contour value demonstrates the atom number in certain distance range (0.1 Å) and angle range (2°). (a) $D = 5$ nm, $E = 2.7$ mJ/cm^2, initial state (before laser energy is applied); (b) $D = 5$ nm, $E = 2.7$ mJ/cm^2; final state; (c) $D = 8$ nm, $E = 2.7$ mJ/cm^2, initial state; (d) $D = 8$ nm, $E = 2.7$ mJ/cm^2, final state; (e) $D = 10$ nm, $E = 2.7$ mJ/cm^2, initial state; (f) $D = 10$ nm, $E = 2.7$ mJ/cm^2, final state; (g) $D = 10$ nm, $E = 2.0$ mJ/cm^2, final state; and (h) $D = 10$ nm, $E = 1.5$ mJ/cm^2, final state. The major tick is every 15° for the angle and 2 Å for the distance. The difference among the initial states for different particles size is small. (b, d, f) Show that the smaller particles are much easier to be twisted. (f, g, h) Inform us that a high laser fluence induces severe twist of particles.

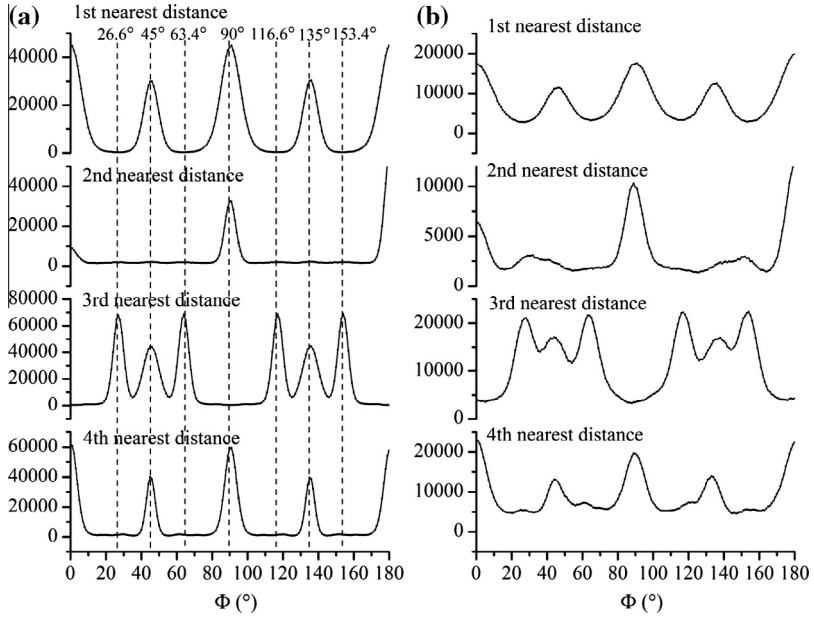

Fig. 9. The angle distribution of the atoms in the 1st–4th order nearest atom distance for $D = 10$ nm, $E = 2.7$ mJ/cm^2. The y axis value is the atom number per degree in the corresponding distance. (a) The angle distribution at the initial state (before the laser energy is applied). Sharp peaks are observed around certain angles which are indicated by the dash lines; and (b) the angle distribution at the final state. The peaks are still visible but less sharp. The atoms are quite broadly distributed in angles compared with (a).

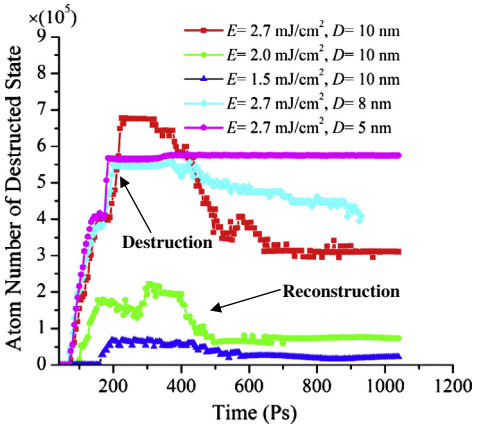

Fig. 10. Evolution of the number of atoms in destructed state against time. Five cases are investigated as indicated in the legend. For the case $D = 5$ nm, $E = 2.7$ mJ/cm^2, the atoms are completely destructed into destructed state and no reconstruction process is observed. In the other 4 cases, reconstruction of the temporarily destroyed structure occurs and the reconstruction number can be viewed as the final plateau value for each case.

The 3rd nearest distance is 6.63 Å. The corresponding angles are 26.6°, 45°, 63.4° and 116.6°, 135°, 153.4°. The 4th nearest distance is 7.66 Å. The corresponding angle are 0°, 45°, 90° and 135°, 180°. The initial state (Fig. 9(a)) is very close to the perfect crystal structure: the peak of each order nearest distance is well located at the corresponding angle and the peak is sharp. At the final state (Fig. 9(b)), the peak is blunt and the distribution is no longer well located around the specific angle, especially for the 3rd nearest distance. The atoms are widely ranged from 26.6° to 63.4° and 116.6° to 153.4°, which is corresponding to the blur region in Fig. 9(f). The crystal structure at final state are twisted to widely spread in the angle regions.

The atom number in the destructed state is studied to reveal the process of compressing. Fig. 10 shows the evolution of the destructed-state atom number against time. The peak point can be viewed as the number of destructed atoms (including temporary and permanent destruction). It is easy to understand that a high laser fluence leads to more destructed atoms when the nanoparticles size are the same where the total atom number is the same. For most cases, the destructed atom number will rise and then fall, which indicates a destruction-then-reconstruction process. However, for the case $D = 5$ nm, $E = 2.7$ mJ/cm^2, the number of destructed atoms will rise and then stay on the plateau value, which means the damage of the crystal structure is mostly a plastic process.

4. Conclusion

In this work, MD simulations were conducted to investigate nanoparticle consolidation by a stress wave induced by pico-second laser ablation of a sacrificial layer. Upon fast laser irradiation, the sacrificial layer quickly melted and phase exploded. Under the constrained domain, the exploded sacrificial layer atoms quickly moved to the nanoparticles and compressed them. Our detailed temperature and structure study revealed that the compression and reconstruction process was rather cold and well below the melting point of the material. On the other hand, destruction and reconstruction took place, and finally cold-sintering of the nanoparticles was achieved. The final cold-sintered structure was found to be nanocrystalline. Smaller nanoparticles were easy to reconstruct, but the final structure was more destructed, and structural defects were observed. For larger particles, the final cold-sintered structure was partially nanocrystalline. The center part of the particle was able to retain its original crystalline structure while consolidation occurred more in the particle–particle contact region. The ODF was developed to investigate the degree of orientation twisting. It was proved to be more comprehensive than RDF in structure analysis for the additional angle information it provides. Our quantitative analysis of the number of reconstructed atoms also showed that the number of reconstructed atoms is higher when the particle size is smaller.

Acknowledgements

Support of this work by the National Science Foundation (Nos. CMMI-1029072 and CMMI-1200397) is gratefully acknowledged.

X.W. thanks the great support of "Taishan Foreign Scholar" program of Shandong Province, China.

References

[1] T. Takiya, I. Umezu, M. Yaga, M. Han, J. Phys: Conf. Ser. 59 (2007) 445.
[2] S. Amoruso, G. Ausanio, R. Bruzzese, M. Vitiello, X. Wang, Phys. Rev. B 71 (2005) 033406.
[3] L.V. Zhigilei, E. Leveugle, B.J. Garrison, Y.G. Yingling, M.I. Zeifman, Chem. Rev. 103 (2003) 321.
[4] A. Plech, V. Kotaidis, M. Lorenc, J. Boneberg, Nat. Phys. 2 (2005) 44.
[5] S. Gacek, X. Wang, Appl. Phys. A 94 (2008) 675.
[6] S. Gacek, X. Wang, J. Appl. Phys. 104 (2008) 126101.
[7] S. Gacek, X. Wang, Phys. Lett. A 373 (2009) 3342.
[8] C. Li, J. Zhang, X. Wang, Appl. Phys. A 112 (2013) 677.
[9] W. Zhang, I.C. Noyan, Y.L. Yao, J. Manuf. Sci. Eng. 126 (2004) 10.
[10] W. Zhang, Y.L. Yao, J. Manuf. Sci. Eng. 124 (2002) 369.
[11] P. Molian, R. Molian, R. Nair, Appl. Surf. Sci. 255 (2009) 3859.
[12] P. Peyre, X. Scherpereel, L. Berthe, C. Carboni, R. Fabbro, G. Béranger, C. Lemaitre, Mater. Sci. Eng., A 280 (2000) 294.
[13] D. Lin, C. Ye, Y. Liao, S. Suslov, R. Liu, G.J. Cheng, J. Appl. Phys. 113 (2013) 133509.
[14] H.K. Amarchinta, R.V. Grandhi, K. Langer, D.S. Stargel, Modell. Simul. Mater. Sci. Eng. 17 (2009) 015010.
[15] J.H. Kim, Y.J. Kim, J.S. Kim, J. Mech. Sci. Technol. 27 (2013) 2025.
[16] W. Braisted, R. Brockman, Int. J. Fatigue 21 (1999) 719.
[17] T. Dunbar, B. Maynard, D.A. Thomas, M.D.M. Peri, I. Varghese, C. Cetinkaya, J. Adhes. Sci. Technol. 21 (2007) 67.
[18] X.K. Shen, J. Sun, H. Ling, Y.F. Lu, Appl. Phys. Lett. 91 (2007) 081501.
[19] X.K. Shen, J. Sun, H. Ling, Y.F. Lu, J. Appl. Phys. 102 (2007) 093301.
[20] L.B. Guo, C.M. Li, W. Hu, Y.S. Zhou, B.Y. Zhang, Z.X. Cai, X.Y. Zeng, Y.F. Lu, Appl. Phys. Lett. 98 (2011) 131501.
[21] R. Nair, W. Jiang, P. Molian, J. Manuf. Sci. Eng. 126 (2004) 637.
[22] S. Plimpton, J. Comput. Phys. 117 (1995) 1.
[23] X. Wang, Y. Lu, J. Appl. Phys. 98 (2005) 114304.
[24] X. Feng, X. Wang, Appl. Surf. Sci. 254 (2008) 4201.
[25] X. Wang, J. Phys. D Appl. Phys. 38 (2005) 1805.